Research Square

Preprints are preliminary reports that have not undergone peer review.
They should not be considered conclusive, used to inform clinical practice,
or referenced by the media as validated information.

Synergistic heating effect via CNT/Fe3O4 nanocomposite aerogels enabling uniform and rapid induction welding with high bond strength in CFRTPs

Nayeong Kim
Korea Institute of Materials Science
Inseok Baek
Korea Institute of Materials Science
Byeongho Park
Korea Institute of Materials Science
Dayoung Kim
Korea Institute of Materials Science
Chaewon Jeong
Korea Institute of Materials Science
Jungwan Lee
Korea Institute of Materials Science
Jung-soo Kim
Korea Institute of Materials Science
Geunsu Joo
Korea Institute of Materials Science
Seokpum Kim
Oak Ridge National Laboratory
Vipin Kumar
Oak Ridge National Laboratory
Youngseok Oh
Korea Institute of Materials Science
Jinsu Kim
jinsu@kims.re.kr

Korea Institute of Materials Science

Research Article

Keywords: Induction welding, Nanocomposites, Aerogels, Joule heating, Hysteresis loss, Carbon nanotubes, Magnetic particles

Posted Date: January 20th, 2026

DOI: https://doi.org/10.21203/rs.3.rs-8372467/v1

License: This work is licensed under a Creative Commons Attribution 4.0 International License. Read Full License

Additional Declarations: No competing interests reported.

Version of Record: A version of this preprint was published at Advanced Composites and Hybrid Materials on September 2nd, 2026. See the published version at https://doi.org/10.1007/s42114-026-02040-x.

Abstract

Effective induction welding of carbon fiber-reinforced thermoplastic composites (CFRTPs) requires both uniform temperature distribution and rapid heating at the welding interface. However, achieving both is challenging because heat localizes due to non-uniform magnetic-field distribution and the difficulty of forming current loops within the composite structure. In this study, a powdered CNT/Fe_3O_4/PA6 aerogel (Nanocomposite) was adopted to enhance induction-heating performance by simultaneously leveraging electrical conductivity and magnetic-loss mechanisms. The nanocomposite contains carbon nanotubes (CNTs) that form continuous conductive pathways, enabling efficient Joule heating and improved heat transfer. The CNTs also act as nanoscale mechanical pins that bridge CFRTPs, thereby enhancing interfacial weld strength. In addition, embedded Fe_3O_4 particles respond rapidly to the alternating magnetic field and act as localized heat sources via magnetic losses, increasing heating efficiency. As a result, the nanocomposite-enabled system demonstrated a 94.6% higher initial heating rate and a 57% reduction in the time required to reach the target processing temperature at the welding interface. The interfacial shear strength increased by 30.8%, and fracture-surface analysis revealed more uniform melting and more effective impregnation across the weld area. These results indicate that the proposed nanocomposite offers a promising strategy for achieving both rapid and uniform heating, leading to improved mechanical performance in the induction welding of CFRTPs.

Highlights

 Proposed a novel nanocomposite aerogel that maximizes induction heating via Joule and magnetic loss mechanisms.

 Incorporated CNTs for Joule heating and FeO for magnetic loss-driven heating enhancement.

 Fabricated nanocomposites with varying ratios and experimentally identified the optimal composition.

 Demonstrated the potential of the proposed material as a high-efficiency nanocomposite for induction welding.

1. Introduction

Induction heating has attracted attention as a welding technique for CFRTPs because it offers rapid heat generation, minimal surface contamination via a non-contact process, and selective heating of targeted areas. Owing to these advantages, induction welding has seen increasing adoption in high-performance sectors such as automotive and aerospace, where rapid and precise joining is essential [1–3]. The efficiency of induction heating is governed by key parameters, including the electrical and magnetic properties of the materials and the continuity of induced-current loops [4]. However, most carbon-fiber-reinforced thermoplastics (CFRTPs) do not satisfy these conditions, leading to induced currents that do not effectively reach the welding interface and difficulty in rapidly attaining the process temperature [5]. In addition, edge effects can cause insufficient melting at the joint center, resulting in incomplete

interfacial fusion and, ultimately, reduced joint strength. Consequently, incorporating a susceptor is essential to maximize the induction-heating effect and to induce selective heat generation at the welding interface [6, 7].

Carbon nanotubes (CNTs) have emerged as promising constituents for induction-assisted joining due to their excellent electrical conductivity and ability to form percolated networks through their high aspect ratio [8]. When exposed to microwaves or high-frequency fields, percolated CNT networks produce Joule heating, thereby supporting more uniform heat generation at the welding interface [9–11]. For example, Cao et al. inserted multiwalled carbon nanotube (MWCNT) sheets at the edges of a carbon fiber heating element to mitigate non-uniform heating, improving overall thermal uniformity [12]. Importantly, the efficacy of CNTs depends strongly on loading level: below the electrical percolation threshold, conduction pathways are sparse and heating is limited, whereas loadings exceeding this threshold result in a rapid increase in network conductivity and heat delivery [13, 14]. However, when the CNT content is increased to excessive levels, dispersion becomes challenging and viscosity increases, which can promote agglomeration, hinder processability, and degrade interfacial uniformity [15]. Moreover, because CNTs are non-magnetic, their heating under alternating magnetic fields is fundamentally less efficient than that of ferromagnetic susceptors [16, 17]. As a result, CNTs are often used as functional reinforcements or auxiliary thermal conductors rather than as primary induction susceptors for welding [18]. Notably, aligned CNT interlayers can significantly enhance interlaminar strength—e.g., improvements of up to 14% and 40% have been reported—while CNT-film electrothermal elements have enabled uniform, rapid consolidation with substantial energy savings [19–21]. Nevertheless, limited magnetic responsiveness and shallow heat penetration constrain the use of CNTs as standalone susceptors in induction systems [22].

Fe_3O_4 is a ferrimagnetic material that heats efficiently via magnetic hysteresis losses when subjected to an alternating magnetic field. Accordingly, Fe_3O_4 has been dispersed in polymer matrices and used as a susceptor for induction heating [23, 24]. For instance, Sha et al. aligned Fe_3O_4 nanoparticles in a Nylon-12 adhesive under an AC magnetic field, boosting the heating rate by up to 200% and enabling reversible joining [25], while Baek et al. achieved stable heating and stable interfacial bonding using PA6 films containing 75 wt% Fe_3O_4 for CF/PA6 induction welding [26]. Although high Fe_3O_4 contents can lead to agglomeration and localized overheating, degrading spatial thermal uniformity [27, 28], design strategies such as particle alignment, architectural control, and hybridization with conductive phases can mitigate these issues [29].

This study deliberately integrates these complementary behaviors in a nanocomposite to achieve both thermal efficiency and interfacial robustness in composite joining. Rather than emphasizing electromagnetic interference (EMI) shielding or purely anisotropic constructs, as in prior CNT/Fe_3O_4 hybrids [30–32], our work focuses on three focal points relevant to induction welding: (i) a powdered CNT/Fe_3O_4/PA6 aerogel interlayer that is simple to process yet conformal to the weld line; (ii) synergistic heating that couples CNT-enabled Joule-heating networks with Fe_3O_4 magnetic hysteresis to flatten

thermal gradients across the interface; and (iii) mechanical reinforcement via CNT anchoring within the resin-rich layer, enhancing interfacial weld strength. The concept is illustrated in Fig. 1 and validated experimentally via heating performance and interfacial mechanical testing. We anticipate that this design provides a practical pathway toward rapid, spatially uniform heating with improved mechanical performance in the induction welding of CFRTPs.

2. Materials and Methods

2.1. Materials

Single-walled carbon nanotubes (SWCNTs, outer diameter 1.6 ± 0.4 nm, length ≥ 5 μm) were purchased from TUBALL® (OCSiAl, Luxembourg). The SWCNTs were ultrasonically dispersed in DI water with Sodium dodecylbenzenesulfonate (Sigma-Aldrich) as a surfactant and used in solution. Magnetite particles (Fe_3O_4, density 4.52 g·cm^{-3}, average particle size ≈ 5 μm) were obtained from Shanghai Laiwu Powder Material Co., Ltd. (China). Polyamide 6 (PA6, density 1.17 g·cm^{-3}, average particle size 15–20 μm) was supplied by Goodfellow (Huntingdon, UK). All materials were employed without additional treatment.

2.2. Induction Heating

Induction heating tests were performed with an induction heater (HF-6K, Taeyang Induction Heater Co., Ltd., Korea). An elliptical, pancake-type copper coil (inner diameter of 3.2 mm) was used; cooling water was circulated through the coil to prevent overheating. The operating frequency and power were set to 300 kHz and 5 kW. The specimen was centered within the coil, with a coil–specimen gap of 2 mm. Specimen temperature was monitored using an infrared thermal imaging camera (FLIR E54, FLIR Systems, Inc., USA).

2.3. Induction Welding Process

Induction welding was carried out using CF/PA6 unidirectional laminate specimens. The specimen dimensions were 101.6 × 25.4 mm^2 with a thickness of 1.81 mm, and the laminate exhibited a fiber volume fraction of 47.3% and a void content of 1.57%. The stacking sequence was $[0/90/\pm45]_{2s}$, fabricated to achieve a quasi-isotropic lay-up. Two specimens were joined in a single-lap configuration with an overlap length of 12.7 mm, and a pressure of 40 kg was applied to the upper adherend during welding. The specimens were mounted in an alumina fixture to maintain alignment. The heating time was set to 70 s, and cooling to room temperature was carried out under pressure.

2.4. Characterization

2.4.1. Characterization of Nanocomposites

A range of characterization techniques was employed to comprehensively evaluate the structural, electrical, and magnetic properties of the nanocomposites. These measurements were conducted to

elucidate how the nanocomposite architecture influences percolation behavior and the electrical and magnetic responsiveness required for induction heating.

Thermogravimetric analysis (TGA; TGA55, TA Instruments, USA) was performed in air at a heating rate of 10°C·min^{-1} up to 600°C, and the Fe_3O_4 residual mass was used to assess how uniformly the Fe_3O_4 particles were distributed along the thickness direction of the aerogel. X-ray micro-computed tomography (micro-CT; vtomex m300, GE, USA) was employed to visualize the three-dimensional dispersion uniformity of Fe_3O_4 particles within the aerogel structure.

Nitrogen adsorption–desorption analysis (BET; iQ 1MP, Quantachrome Instruments, USA) was performed on powdered aerogels to verify their specific surface area and to evaluate nitrogen adsorption and desorption behavior through the isotherm graph.

Electrical conductivity was measured using a four-point probe (FPP-2000, DASOL ENG, Korea) on hot-pressed films (25.4 × 12.7 mm^2) to examine how Fe_3O_4 loading affects the formation of CNT percolation networks. Vibrating sample magnetometry (VSM; MicroSense EZ VSM, MicroSense, USA) was conducted under an applied magnetic field of ± 25 kOe to analyze the magnetic responsiveness of the nanocomposites, with particular emphasis on determining how well the Fe_3O_4-based magnetic response is retained upon CNT incorporation.

Field-emission scanning electron microscopy (FE-SEM; JSM-7800F, JEOL, Japan) was used to observe the porous aerogel microstructure and to verify the formation of interconnected CNT/Fe_3O_4 networks that define the structural characteristics of the interlayer.

2.4.2. Characterization of Welded joints

To evaluate the reliability of the welded joints, a series of non-destructive, mechanical, and microstructural analyses were performed. Non-destructive CT inspection was further conducted to assess the integrity of the welded interface. For this evaluation, a Phoenix Vtomex M240 system equipped with a micro-focus X-ray tube was operated at 60 kV and 180 μA. The voxel resolution was set to 10 μm to enable precise detection of interfacial defects, and a total of 2,200 projection images were collected and reconstructed into a three-dimensional CT volume. In addition, immersion ultrasonic C-scan mapping was performed using a TTU system (GTR4010-ARN-CA) to evaluate the continuity and uniformity of the welded region across the entire bonded area, and to detect internal defects such as lack of fusion through area-based attenuation signals.

Single-lap shear (SLS) tests were conducted according to ASTM D5868 at a crosshead speed of 1 mm·min^{-1}, using $n \geq 3$ specimens per condition to ensure reproducibility. These tests were used to compare the mechanical strength improvement achieved by incorporating the nanocomposite interlayer relative to the CFRP-only joints.

Field-emission scanning electron microscopy (FE-SEM; JSM-7800F, JEOL, Japan) was employed to observe CNT pull-out features on the fracture surfaces, enabling analysis of interfacial failure behavior and the contribution of CNT anchoring to the mechanical performance of the welded joints.

3. Results and discussion

3.1. Fabrication and Microstructure of CNT/Fe_3O_4/PA6 Nanocomposite aerogel

To achieve rapid and spatially uniform induction heating, both conductive pathways and magnetically responsive particles must be homogeneously distributed through the nanocomposite architecture. We therefore prepared a CNT/Fe_3O_4/PA6 nanocomposite via an aqueous route followed by rapid freezing and vacuum freeze-drying. The process yielded aerogels that were readily shaped into arbitrary geometries without cracking (Fig. 2c) and possessed exceptionally low density due to their percolated pore network (Fig. 2d). This aerogel form factor offered practical advantages for welding: it can be trimmed to a conformal interlayers that match the weld line, handled and transferred with minimal mass loading, and, if needed, gently milled into a powdered aerogel while retaining the underlying CNT–Fe_3O_4 connectivity. Accordingly, single-walled CNTs were individually dispersed in water with an surfactant and then mixed with Fe_3O_4 and PA6 powders; the powder-dispersed solution was quenched in liquid nitrogen to grow ice crystals and lyophilized (− 120°C, 24 h), during which solvent sublimation generated the porous aerogel (Fig. 2a).

The freeze-drying route mitigated sedimentation of relatively dense Fe_3O_4 during solvent removal, which enabled a uniform through-thickness distribution within the CNT scaffold. To quantify compositional uniformity, thermogravimetric analysis (TGA) was performed on sections taken from the top and bottom of the aerogel. The residual masses were 36.4% and 37.2%, respectively, corresponding to a difference of only ~ 0.8%, which confirmed that particle settling was effectively suppressed during processing. Complementary X-ray micro-computed tomography (micro-CT) revealed a homogeneous three-dimensional dispersion of Fe_3O_4 throughout the aerogel volume, consistent with the TGA results (Fig. 2e, f).

Microstructural observations supported the formation of a dual-loss nanocomposite network. Field-emission SEM images showed an open, vertically porous architecture characteristic of freeze-dried structures (Fig. 2b). Additional microstructural features of the aerogel monolith are provided (see Fig. S1 in the Supplementary data). Within this porous network, Fe_3O_4 particles were embedded and wrapped by CNT bundles to form an interconnected percolation network (Fig. 2g). This architecture was expected to (i) provide continuous electronic pathways for distributed Joule heating via the CNT network and (ii) supply numerous, well-dispersed magnetic nano/microsources for hysteresis-based heat generation via Fe_3O_4 under an alternating field. The intimate CNT–Fe_3O_4 contact further facilitated heat sharing across phases and promoted mechanical interlocking (“pinning”) of CNTs within the resin-rich layer after

deposition, establishing a structural basis for both uniform thermal fields and enhanced interfacial bond strength during induction welding.

The CNT/Fe_3O_4/PA6 nanocomposites were prepared with varying compositions, and the samples were designated based on their component combination. In the sample codes, C, F, and P represented CNT, Fe_3O_4, and PA6, respectively, and the following number indicated the PA6 content (wt%). The detailed compositions are summarized in Table 1.

Table 1
Composition of CNT/Fe_3O_4/PA6 nanocomposite samples.

Sample	CNT (wt%)	Fe_3O_4 (wt%)	PA6 (wt%)
FP	-	100	100
CFP0	100	100	-
CFP10	100	100	10
CFP30	100	100	30
CFP50	100	100	50

Nitrogen adsorption–desorption analysis showed that the powdered aerogel had a specific surface area of 104.24 $m^2 \cdot g^{-1}$ (Fig. 3a). This value is significantly higher than the specific surface area range of carbon fibers (CF), which is 0.5–5 $m^2 \cdot g^{-1}$. Therefore, the powdered aerogel provides more pathways for resin infiltration compared to using only carbon fiber composites, and the open pore structure allows for more efficient resin penetration into the internal pores. As a result, it is anticipated that resin impregnation will occur more effectively, leading to an enhancement in interfacial welding strength.

Electrical conductivity measurements, performed at a fixed CNT:PA6 ratio of 1:0.5, showed a non-monotonic dependence of bulk conductivity (σ) on Fe_3O_4 loading (Fig. 3b). In Regime I, the introduction of Fe_3O_4 initially reduced σ because the relative CNT content decreased, and some tube–tube junctions were obstructed (dilution/blocked-junction effect). Beyond the percolation threshold of Fe_3O_4, Regime II emerged: σ increased again as Fe_3O_4 participated in assisted percolation, effectively bridging separated CNT domains and restoring long-range connectivity. The composition with equal masses of CNT and Fe_3O_4 (CFP50) delivered the highest conductivity, 3347.92 $S \cdot m^{-1}$, consistent with an optimally connected hybrid network capable of distributing Joule heat uniformly along the weld line. The two regimes were summarized schematically in Fig. 3c.

Magnetic characterization by VSM, normalized by the Fe_3O_4 mass, confirmed that ferrimagnetic behavior was retained after hybridization with CNT and PA6 (Fig. 3d; Table 2). Bare Fe_3O_4 showed M_s = 70.59 $emu \cdot g^{-1}$. Mixing Fe_3O_4 with PA6 at equal mass decreased M_s by only 7.77%, indicating minimal

magnetic interference from the polymer. In contrast, CNT-containing hybrids displayed a larger reduction in M_s—up to 53.93%—which we ascribed to interfacial charge transfer and spin disorder at CNT/Fe_3O_4 contacts that weakened exchange interactions. Notably, the electrically optimal composition (CFP50) still retained substantial magnetization, yielding a balanced electro-magnetic profile: percolated CNT pathways for heat spreading via Joule heating together with Fe_3O_4-driven hysteresis losses for rapid local heat generation.

Table 2
Summary of VSM magnetization results

Sample	Magnetization ($emu \cdot g^{-1}$)	Reduction vs. bare Fe_3O_4 (%)
Bare Fe_3O_4	70.59	-
FP	65.11	7.77
CFP0	34.77	70.74
CFP50	32.53	53.93

Taken together, the BET, conductivity, and magnetization results demonstrated that the powdered nanocomposite aerogel (CFP50) promoted interfacial contact, restored conductive percolation at optimal Fe_3O_4 loadings, and preserved sufficient magnetic response. This combination is precisely what is required to achieve rapid yet spatially uniform induction heating and high interfacial bond strength in CFRTP welding.

3.2. Induction Heating Performance of the Nanocomposite

We assessed the nanocomposite as an active heating material by quantifying heating efficiency and spatial uniformity under a kilohertz alternating magnetic field (Fig. 4). To probe whether electronic and magnetic loss channels acted cooperatively, CNT-only aerogels were compared with CNT/Fe_3O_4/PA6 hybrids. Over a 60 s induction period, the hybrid consistently reached higher peak temperatures than CNT-only (Fig. 4a). The best performance occurred when CNT, Fe_3O_4, and PA6 were all present at CFP50, indicating that Joule losses in the percolated CNT network and magnetothermal losses (hysteresis/relaxation) in Fe_3O_4 are mutually reinforcing, with dielectric dissipation in PA6 providing a smaller but beneficial contribution [33, 34].

To isolate the role of the polymer, the CNT:Fe_3O_4 mass ratio was fixed at 1:1 while PA6 content was varied (Fig. 4b). Increasing PA6 led to a monotonic decrease in peak temperature, consistent with the dilution of the conductive skeleton and a reduced relative contribution from the CNT/Fe_3O_4 network at high polymer fractions. Thus, although PA6 contributes measurable dielectric loss near processing temperatures, excess polymer penalizes overall heating efficiency by lowering the effective density of current paths and magnetic heat sources.

Heating uniformity was examined by infrared thermography (Fig. 4c,d). At CFP50, the nanocomposite aerogel exhibited a spatially uniform temperature field above the PA6 melting point without obvious hot spots (Fig. 4c), consistent with balanced power deposition from electronic and magnetic losses and subsequent smoothing by thermal diffusion through a continuous polymer phase. The temperature non-uniformity index, calculated from the IR thermography data, was 10.89%, further confirming the spatially uniform interfacial heating. In contrast, at CFP10, hot spots emerged (Fig. 4d), attributable to insufficient dielectric participation and heat spreading, which concentrate power in highly conductive or strongly magnetic locales. The uniformity trend aligns with the peak-temperature optimum near CFP50 (Fig. 4a) and the decline at higher polymer contents (Fig. 4b).

Early-time responsiveness was benchmarked using the initial heating rate (Fig. 4e). Under identical inputs, CFRP-only showed little rate gain with voltage, whereas the nanocomposite aerogels responded sharply; at 170 V the maximum initial rate reached 148.7°C·s^{-1}, which was 94.6% higher than CFRP-only. This contrast reflects the lack of closed induced-current loops in CFRP (dielectric-loss-dominated) versus the percolated, closed-loop network in the nanocomposite aerogel.

Finally, to simulate the welding process, the nanocomposite aerogel was deployed as a thin interlayer laminated on CFRP (Fig. 4f). Relative to CFRP-only, overlaying the laminate with the nanocomposite aerogel increased the initial heating rate from 43.7 to 68.6°C·s^{-1} (~ 57%), the time to reach the processing temperature was markedly shorter, and the temperature at t = 20 s was up to 173°C higher under the same input. These results demonstrate that the CNT/Fe_3O_4/PA6 nanocomposite accelerates heating while flattening thermal gradients, thereby improving process efficiency and establishing favorable thermal conditions for strong, uniform induction-welded joints.

3.3. Application to Induction Welding

The powdered aerogel nanocomposite (CFP50) was inserted as a thin interlayer in single-lap CFRP joints (Fig. 5a,b) to evaluate whether the improved heating efficiency and spatial uniformity (Fig. 4) translated into reliable joints. Welding was performed in an alumina fixture to maintain alignment.

To evaluate the reliability of the weld interface, micro-CT analyses were conducted from both cross-sectional and top-view perspectives. In the CFRP-only specimen, the cross-section revealed incomplete joining with noticeable delamination regions, and in the top view, a central defect was observed, indicating the presence of unwelded areas (Fig. S2). These unwelded regions were attributed to non-uniform melting during heating. In contrast, the CFP50 specimen exhibited no delamination at the joint interface, and Fe_3O_4 particles dispersed within the powdered aerogel were clearly observed (Fig. 5c). The small voids formed near the welding line appeared to originate from the rapid melting of the CFRP matrix during induction heating; however, no separation or lifting of the welded line was observed after solidification. Furthermore, in the top view, unlike the CFRP-only specimen, the welding interface exhibited uniform melting, and Fe_3O_4 particles were uniformly distributed throughout the entire welding region (Fig. 5d). Taken together, the observations demonstrated that the CNT/Fe_3O_4/PA6 nanocomposite

acted as an effective thermal mediator during induction heating, facilitating the formation of a uniform and stable interface.

The transmission ultrasonic inspection results (Table 3) revealed a clear distinction between the CFRP-only joints and the joints incorporating nanocomposites with different PA6 contents. In the Figure legend (Fig. 5g), the red color can be regarded as the reference signal corresponding to 100% transmission, whereas darker colors indicate a progressive decrease in relative ultrasonic transmission. The CFRP-only joint exhibited a transmission ratio of only 6% at 57 dB, indicating that ultrasonic waves were largely attenuated even under relatively high input, and continuous transmission across the interface was not achieved. In the C-scan images, a distinct boundary was observed between the edge and center regions, suggesting that a significant portion of the joint interface was non-uniformly or incompletely welded. In contrast, the joints with nanocomposites (CFP10 and CFP50) exhibited transmission ratios of 41% and 43% at comparable dB levels (55–60 dB), confirming continuous and uniform ultrasonic transmission throughout the overlap region. These results demonstrate that, even when considering differences in dB settings, the nanocomposite-containing joints showed significantly higher transmission ratios than the CFRP-only joints, suggesting that the incorporation of nanocomposites improved interfacial uniformity and stabilized the ultrasonic propagation path, thereby promoting spatially uniform welding. Although ultrasonic transmission characteristics do not directly correspond to mechanical strength, combined interpretation with mechanical tests is required to draw comprehensive conclusions. Nevertheless, the increased transmission can be interpreted as evidence of improved interfacial uniformity. Furthermore, it should be noted that a decrease in ultrasonic transmission cannot always be solely attributed to interfacial defects, but may also arise from structural factors such as increased joint thickness or the fiber stacking sequence of the CFRP.

Table 3
Ultrasonic transmission results of CFRP-only and nanocomposite joints.

Sample	dB	Transmission ratio (%)
CFRP-only	57	6
With CFP0	62	25
With CFP10	60	41
With CFP50	55	43

To verify the mechanical reinforcement effect of the nanocomposite (CFP50), fracture surfaces were examined after single-lap shear testing. Relative to the CFRP-only, the nanocomposite afforded faster interfacial heating and more uniform melting across the weldline, as indicated by the absence of visually unmelted central regions after welding (Fig. 6b). Correspondingly, the single-lap shear strength increased from 19.21 MPa (CFRP-only) to 25.12 MPa with the nanocomposite (+ 30.8%; Fig. 6a). We attribute this gain to (i) balanced power deposition from Joule and hysteresis losses that flattens the thermal gradient

and promotes uniform fusion, and (ii) CNT-mediated load transfer, whereby nanotube bundles embedded in the resin-rich layer act as “pins,” improving interfacial traction under shear.

To elucidate the microstructural origins of strength improvement, we examined fracture surfaces by FE-SEM (Fig. 7). Prior to induction heating, the powdered aerogel nanocomposite showed a distinct granular/layered morphology at the interface (Fig. 7a). After welding, PA6 infiltration was evident along the CNT–Fe_3O_4 network (Fig. 7b), indicating intimate wetting and co-melting between the interlayer and the CFRTP resin. High-magnification images (Fig. 7c–e) all showed CNT pull-outs. Figure 7c revealed that CNTs were uniformly pulled out over a wide area of the joint interface, while Fig. 7d provided a magnified view of this region for more detailed observation. Figure 7e presented an even higher magnification, clearly showing individual CNT strands fully pulled out. These CNT pull-outs and bridging ligaments are indicative of effective mechanical interlocking and energy dissipation during loading and, together with the uniform thermal field established during welding, rationalize the observed enhancement in lap-shear strength.

Overall, the CNT/Fe_3O_4/PA6 nanocomposite functions as an electromagnetically balanced heating material that accelerates heating, equalizes temperature across the overlap, and reinforces the interface at multiple length scales. This combination yields stronger and more reliable induction-welded CFRP joints.

3.4. Proposed Heating and welding Mechanism

In an alternating (kHz) magnetic field, the nanocomposite dissipates energy via three coupled channels (Fig. 8a): (i) Joule heating in the percolated CNT network that establishes low-impedance pathways; (ii) magnetic hysteresis/relaxation losses in Fe_3O_4 that provide volumetric magnetothermal heating in the RF/kHz regime; and (iii) dielectric loss in PA6 that becomes non-negligible near processing temperatures. The coexistence of conductive and magnetic pathways increases the effective loss factor and explains the higher initial heating propensity and shorter time-to-melt relative to single-mode heating materials. This interpretation agrees with polymer induction-processing literature (magnetite susceptors operated near ~ 100 kHz for welding) [35] and with reports that CNT networks enable efficient electrothermal self-heating [36], while Fe_3O_4 particles heat through hysteresis/relaxation under comparable frequencies [37–40].

The freeze-dried then powdered aerogel morphology increases accessible surface area and packability at the weldline, improving thermal/physical contact and enabling conformal placement in local gaps (our measurements) (Fig. 8b). In parallel, the uniform Fe_3O_4 distribution within the CNT network mitigates current hot-spots and spreads magnetic losses, flattening temperature gradients—consistent with the IR thermography uniformity observed here and with studies showing heating efficiency/uniformity are dispersion-controlled in magnetically susceptible nanocomposites.

During welding, uniformly heated PA6 melts and infiltrates the overlap, while interfacial CNT filaments act as nanoscale pins/bridges, enhancing load transfer and resisting interfacial crack growth via pull-

out/bridging—mechanisms widely reported to raise interlaminar toughness in CNT-modified joints and laminates [41] (Fig. 8c). The combination of magnetothermal efficiency (Fe_3O_4) and interfacial toughening (CNT) is consistent with induction-welded thermoplastic systems employing magnetite-based susceptors.

4. Conclusions

We demonstrated that a powdered CNT/Fe_3O_4/PA6 nanocomposite enables uniform and rapid induction heating for polymer–composite welding. When subjected to an alternating magnetic field, the percolated CNT network provides efficient Joule heating, Fe_3O_4 contributes magnetothermal losses (hysteresis/relaxation), and PA6 adds dielectric dissipation; together these loss channels produce spatially uniform interfacial temperatures and robust weld quality. The powdered aerogel morphology increases accessible surface area and packability at the overlap, improving thermal/physical contact and facilitating conformal placement, which results in more homogeneous melting and infiltration across the joint.

Quantitatively, the nanocomposite increased the initial heating rate to 148.7°C·s^{-1}, and shortened the time-to-T□□□□ by 57%. IR thermography indicated that the temperature non-uniformity index was 10.89%, consistent with the uniform interfacial temperature field. In terms of mechanical performance, the lap-shear strength increased from 19.21 MPa to 25.12 MPa. Fractography revealed CNT pull-out and bridging, supporting an interfacial pinning mechanism for the observed strength gains.

The proposed nanocomposite offers a drop-in route to uniform, fast induction welding using off-the-shelf kHz systems and gram-scale material usage, enabling scalable and selective repairs or assembly of thermoplastic-rich interfaces. By engineering loss partitioning and leveraging IR-guided digital twins for temperature-field control—then by extending the concept across materials and lay-ups—the approach can evolve into a robust, deployable joining platform.

Declarations

Declaration of competing interest

The authors declare that they have no known competing financial interests or personal relationships that could have appeared to influence the work reported in this paper.

Funding

This work was supported by the National Research Foundation of Korea (NRF) grants funded by the Korea government (No. NRF- 2022M3H4A1A0407637213, RS-2024-00448445),

and Korea Institute of Materials Science (PNKA400).

Author Contribution

Nayeong Kim: Writing – original draft, Methodology, Visualization. Inseok Baek: Writing – original draft, Methodology, Visualization. Byeongho Park: Investigation, Resources. Dayoung Kim: Investigation, Resources. Jungwan Lee: Data curation, Review manuscript. Jin Woo Yi: Data curation, Review manuscript. Jung-soo Kim: Investigation, Data curation. Geunsu Joo: Investigation, Data curation. Seokpum Kim: Review manuscript. Vipin Kumar: Review manuscript. Youngseok Oh: Supervision, Project administration, Conceptualization, Funding acquisition, Methodology. Jinsu Kim: Spervision, Resources, Review & editing manuscript.

Acknowledgement

This work was supported by the National Research Foundation of Korea (NRF) grants funded by the Korea government (No. NRF- 2022M3H4A1A0407637213, RS-2024-00448445), and Korea Institute of Materials Science (PNKA400).

References

1. Ahmed TJ, Stavrov D, Bersee HEN, Beukers A. Induction welding of thermoplastic composites—an overview. *Compos. Part A: Appl. Sci. Manuf.* 2006;37:1638–1651.
2. Liu J, Quan D, Scarselli G, Alderliesten R, Wang H, Zhao G. Developments and future prospects of welding technology for carbon fiber thermoplastic composites. *Compos. Part B: Eng.* 2025;297:112314.
3. Bayerl T, Duhovic M, Mitschang P, Bhattacharyya D. The heating of polymer composites by electromagnetic induction – A review. *Compos. Part A: Appl. Sci. Manuf*. 2014;57:27–40.
4. Farahani RD, Dubé M. Novel heating elements for induction welding of carbon fiber/polyphenylene sulfide thermoplastic composites. *Adv. Eng. Mater.* 2017;19:1700196.
5. Gouin O'Shaughnessey P, Dubé M, Fernandez Villegas I. Modeling and experimental investigation of induction welding of thermoplastic composites and comparison with other welding processes. *J. Compos. Mater.* 2016;50:2895–2910.
6. Vattathurvalappil SH, Haq M. Thermomechanical characterization of Nano-Fe_3O_4 reinforced thermoplastic adhesives and single lap-joints. *Compos. Part B: Eng.* 2019;175:107128.
7. Roman CL, da Silva Moura N, Wicker S, Dooley KM, Dorman JA. Induction heating of magnetically susceptible nanoparticles for enhanced hydrogenation of oleic acid. *ACS Appl. Nano Mater.* 2022;5:3676–3685.

8. Bryning MB, Milkie DE, Islam MF, Hough LA, Kikkawa JM, Yodh AG. Carbon nanotube aerogels. *Adv. Mater.* 2007;19:661–664.
9. Sweeney CB, Lackey BA, Pospisil MJ, Achee TC, Hicks VK, Moran AG, Teipel BR, Saed MA, Green MJ. Welding of 3D-printed carbon nanotube–polymer composites by locally induced microwave heating. *Sci. Adv.* 2017;3:e1700262.
10. Wang F, Zhang P, Luo J, Li B, Liu G, Zhan X. Effect of heat input on temperature characteristics and fusion behavior at bonding interface of CFRTP induction welded joint with carbon fiber susceptor. *Polym. Compos.* 2022;44:1586–1602.
11. Poyraz S, Zhang L, Schroder A, Zhang X. Ultrafast microwave welding/reinforcing approach at the interface of thermoplastic materials. *ACS Appl. Mater. Interfaces* 2015;7:22469–22477.
12. Cao D. Fusion joining of thermoplastic composites with a carbon fabric heating element modified by multiwalled carbon nanotube sheets. *Int. J. Adv. Manuf. Technol.* 2023;128:4443–4453.
13. Marconnet AM, Yamamoto N, Panzer MA, Wardle BL, Goodson KE. Thermal conduction in aligned carbon nanotube–polymer nanocomposites with high packing density. *ACS Nano* 2011;5:4818–4825.
14. Karalis G, Tzounis L, Dimos E, Mytafides CK, Liebscher M, Karydis-Messinis A, et al. Printed single-wall carbon nanotube-based Joule heating devices integrated as functional laminae in advanced composites. *ACS Appl. Mater. Interfaces* 2021;13:39880–39893.
15. Islam MF, Rojas E, Bergey DM, Johnson AT, Yodh AG. High weight fraction surfactant solubilization of single-wall carbon nanotubes in water. *Nano Lett*. 2003;3:269–273.
16. Ma M, Wu Y, Zhou J, Sun Y, Zhang Y, Gu N. Size dependence of specific power absorption of Fe_3O_4 particles in AC magnetic field. *J. Magn. Magn. Mater.* 2004;268:33–39.
17. Martin RG, Johansson C, Tavares JR, Dubé M. Material selection methodology for an induction welding magnetic susceptor based on hysteresis losses. *Adv. Eng. Mater.* 2021;24:2100739.
18. Li X, Li M, Peng W, Li C, Yi J, Zhao L, et al. Orientation adaptive heterogeneous CNT/Fe_3O_4 composite membrane with excellent Joule heating and enhanced electromagnetic shielding properties. *J. Mater. Sci.* 2024;59:16583–16603.
19. Guzman de Villoria R, Hallander P, Ydrefors L, Nordin P, Wardle BL. In-plane strength enhancement of laminated composites via aligned carbon nanotube interlaminar reinforcement. *Compos. Sci. Technol.* 2016;133:33–39.
20. Ni X, Furtado C, Kalfon-Cohen E, Zhou Y, Valdes GA, Hank TJ, et al. Static and fatigue interlaminar shear reinforcement in aligned carbon nanotube-reinforced hierarchical advanced composites. *Compos. Part A: Appl. Sci. Manuf.* 2019;120:106–115.
21. Li X, Daso F, Lee J, Spangler J, Canart J-P, Kinsella M, et al. Consolidation of aerospace-grade high-temperature thermoplastic carbon fiber composites via nano-engineered electrothermal heating. *Compos. Part B: Eng.* 2023;262:110781.
22. Rudolf R, Mitschang P, Neitzel M. Induction heating of continuous carbon-fibre-reinforced thermoplastics. *Compos. Part A: Appl. Sci. Manuf.* 2000;31:1191–1202.

23. Cheng X, Zhou Y, Charles ADM, Yu Y, Islam MS, Peng S, et al. Enabling contactless rapid on-demand debonding and rebonding using hysteresis heating of ferrimagnetic nanoparticles. *Mater. Des.* 2021;210:110071.
24. Sha Z, Cheng X, Zhou Y, Rider AN, Charles ADM, Chang W, et al. Simultaneous improvement of heating efficiency and mechanical strength of a self-healing thermoplastic polymer by hybridizing magnetic particles with conductive fibres. *Compos. Part A: Appl. Sci. Manuf.* 2023;172:107257.
25. Sha Z, Cheng X, Charles ADM, Zhou Y, Islam MS, Rider AN, et al. In-situ aligning magnetic nanoparticles in thermoplastic adhesives for contactless rapid joining of composite structures. *Compos. Struct.* 2023;321:117324.
26. Baek I, Lee S. A study of films incorporating magnetite nanoparticles as susceptors for induction welding of carbon fiber reinforced thermoplastic. *Mater. (Basel)* 2020;13:457.
27. Bae D, Shin P, Kwak S, Moon M, Shon M, Oh S, et al. Heating behavior of ferromagnetic Fe particle-embedded thermoplastic polyurethane adhesive film by induction heating. *J. Ind. Eng. Chem.* 2015;30:92–97.
28. Vattathurvalappil SH, Kundurthi S, Drzal LT, Haq M. Thermo-mechanical degradation in ABS-Fe_3O_4 polymer nanocomposite due to repeated electromagnetic heating. *Compos. Part B: Eng.* 2020;201:108364.
29. Liu K, Han L, Tang P, Yang K, Gan D, Wang X, et al. An anisotropic hydrogel based on mussel-inspired conductive ferrofluid composed of electromagnetic nanohybrids. *Nano Lett.* 2019;19:8343–8356.
30. Zhang B, Qu Z, Ruiz-Agudo C, Yang L, Chi B, Kong Y, et al. Lightweight magnetic carbon nanotube/cellulose nanofibre aerogels with microstructure engineering for enhanced microwave absorption. *Carbon* 2025;234:119652.
31. Wang X, Zhao Z, Qu J, Wang Z, Qiu J. Fabrication and characterization of magnetic Fe_3O_4–CNT composites. *J. Phys. Chem. Solids* 2010;71:673–676.
32. Rajagukguk J, Simamora P, Saragih CS, Abdullah H, Gultom NS, Imaduddin A, et al. Superparamagnetic behaviour and surface analysis of Fe_3O_4/PPY/CNT nanocomposites. *J. Nanomater.* 2020;2020:8896243.
33. Li M, Wen L, Wang S, Liang J, Hou X. Heat generation mechanisms during induction heating of cross-ply carbon fiber reinforced thermoplastic laminates. *Polym. Test.* 2024;130:108318.
34. Becker S, Michel M, Mitschang P, Duhovic M. Influence of polymer matrix on the induction heating behavior of CFRPC laminates. *Compos. Part B: Eng.* 2022;231:109538.
35. Miller SG, et al. Assessment of thermoplastic composite joining by induction welding (NASA TM-20250006527). NASA 2025.
36. Rosensweig RE. Heating magnetic fluid with alternating magnetic field. *J. Magn. Magn. Mater.* 2002;252:370–374.
37. Dennis CL, Ivkov R. Physics of heat generation using magnetic nanoparticles for hyperthermia. *Int. J. Hyperthermia* 2013;29:715–729.

38. Shah RR, Davis TP, Glover AL, Nikles DE, Brazel CS. Impact of magnetic field parameters and iron oxide nanoparticle properties on heat generation for use in magnetic hyperthermia. *J. Magn. Magn. Mater.* 2015;387:96–106.
39. Sun Y, Davis E. Nanoplatforms for targeted stimuli-responsive drug delivery: A review of platform materials and stimuli-responsive release and targeting mechanisms. *Nanomaterials (Basel)* 2021;11:746.
40. Obaidat IM, Issa B, Haik Y. Magnetic properties of magnetic nanoparticles for efficient hyperthermia. *Nanomaterials (Basel)* 2015;5:63–89.
41. Gude MR, Prolongo SG, Ureña A. Toughening effect of carbon nanotubes and carbon nanofibres in epoxy adhesives for joining carbon fibre laminates. *Int. J. Adhes. Adhes.* 2015;62:139–145.

Figures

Figures

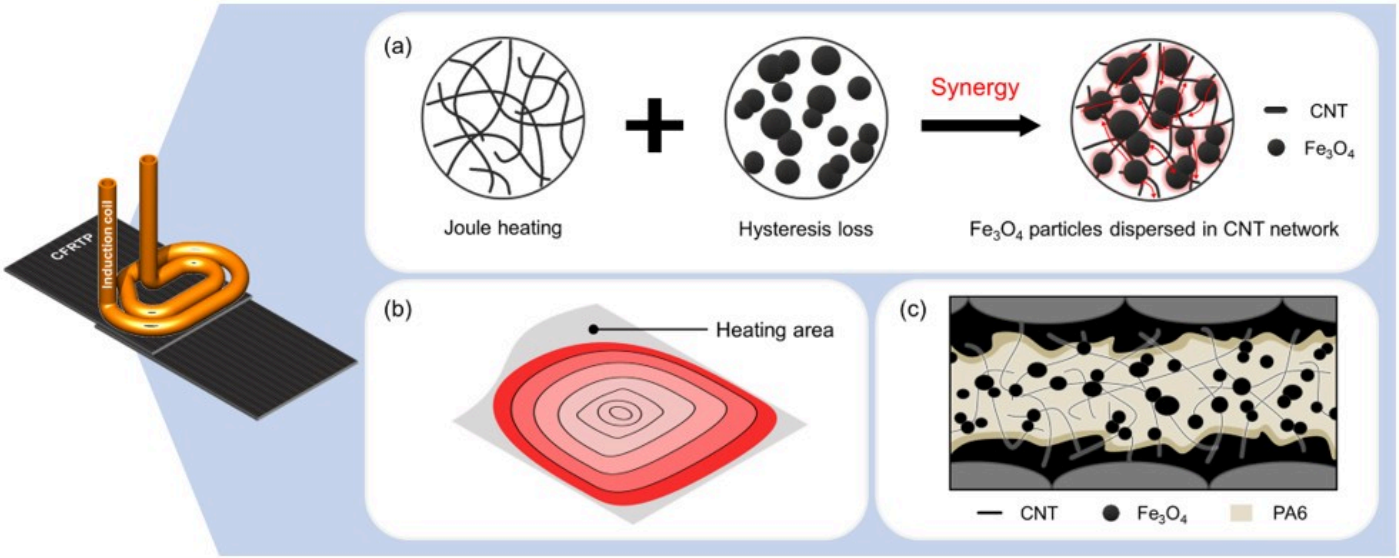


Figure 1

Schematic illustration of the CNT/Fe_3O_4 nanocomposite aerogel for CFRTP induction welding: (a) synergistic heating effect; (b) uniform heat distribution; (c) CNT pinning effect enhancing interfacial bonding.

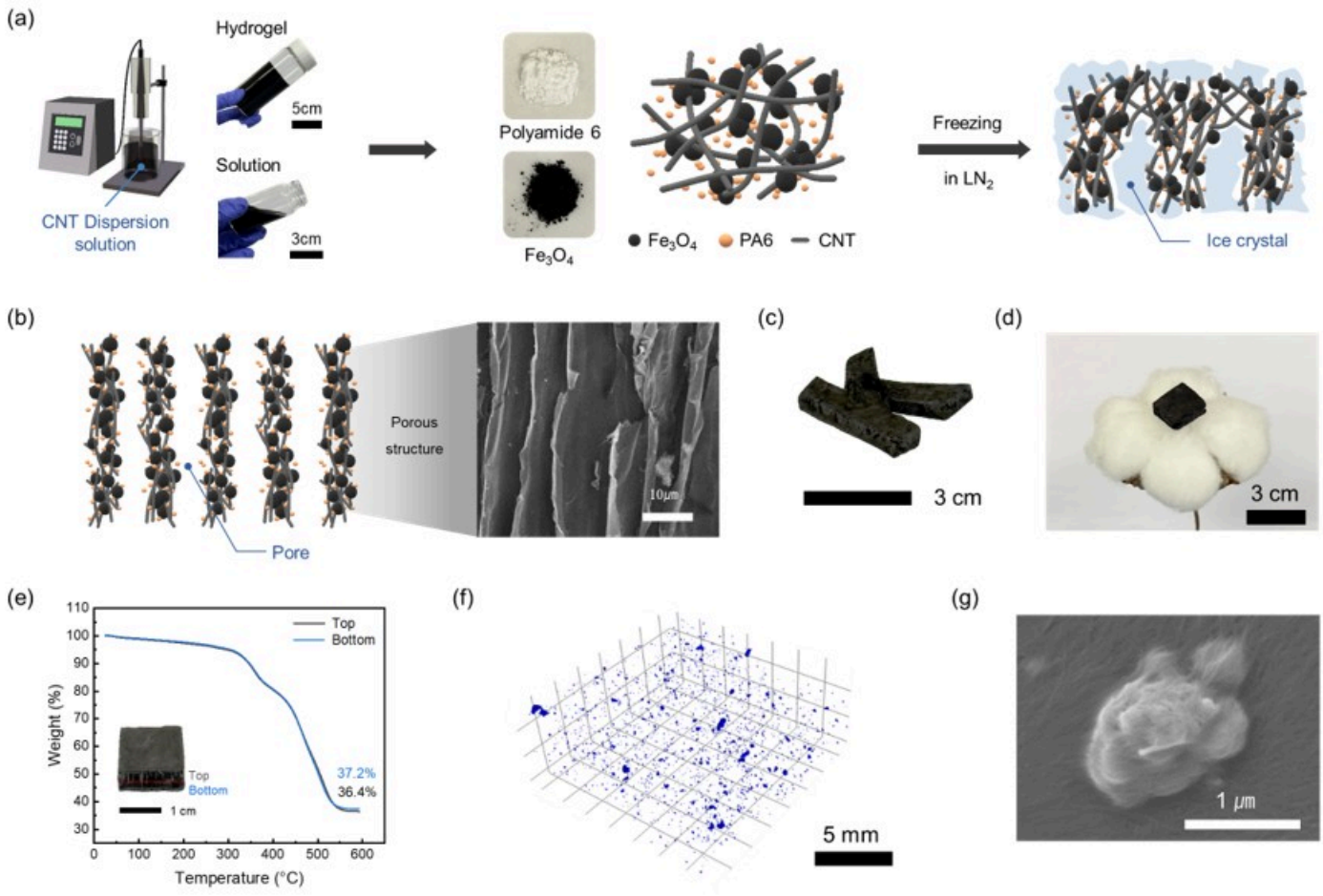


Figure 2

Freeze-dried CNT/Fe_3O_4/PA6 aerogel: (a) schematic of freeze drying process; (b) porous aerogel morphology; (c) fabricated shapes; (d) lightweight property; (e) Fe_3O_4 distribution through the thickness (TGA); (f) Fe_3O_4 distribution (3D micro-CT); (g) formation of CNT–Fe_3O_4 network (FE-SEM).

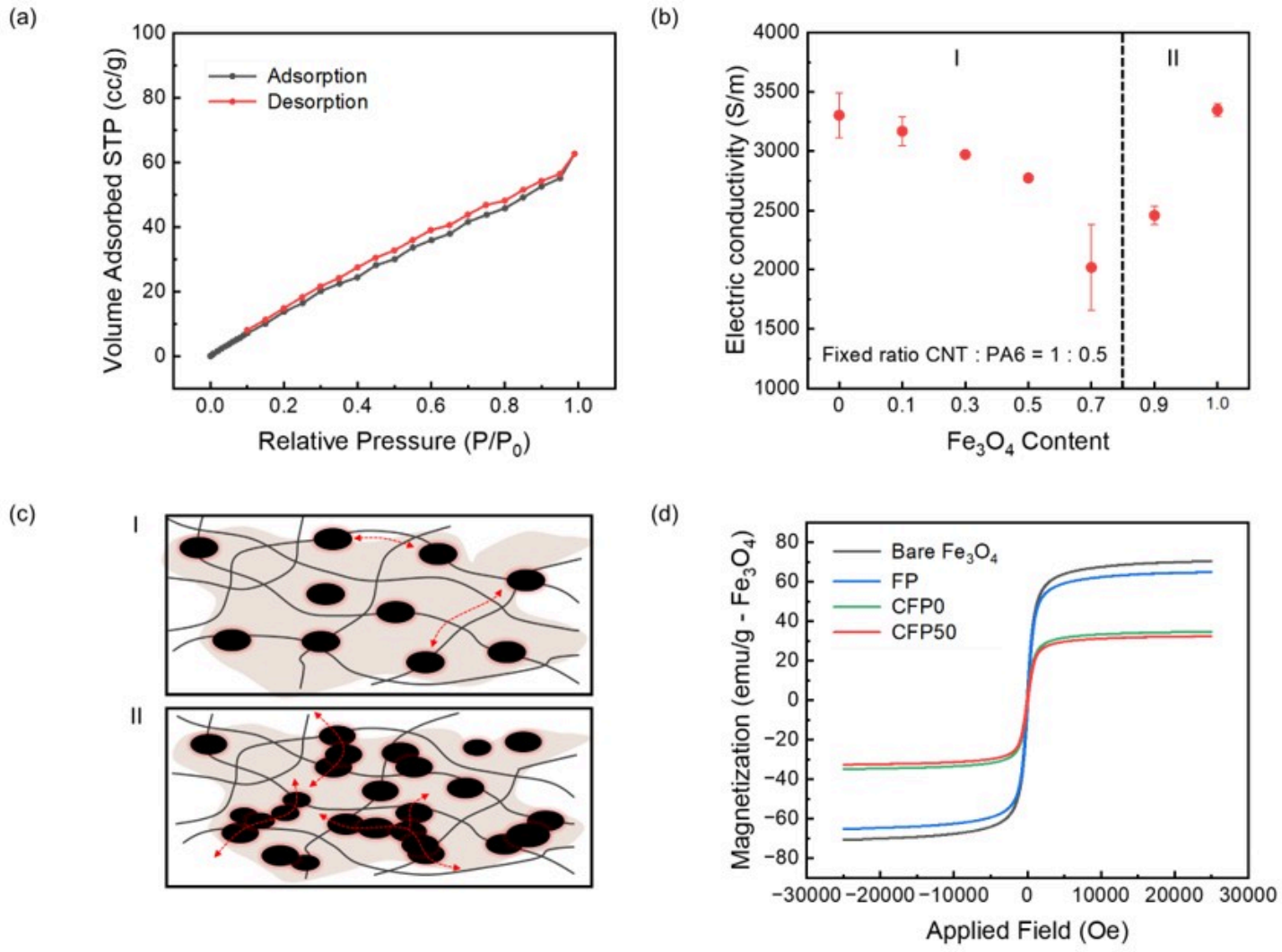


Figure 3

Characterization of CNT/Fe_3O_4/PA6 nanocomposites: (a) Nitrogen adsorption–desorption isotherm of the powdered aerogel; (b) electrical conductivity as a function of Fe_3O_4 content; (c) schematic of Regime I and II conduction mechanisms; (d) VSM M–H curves.

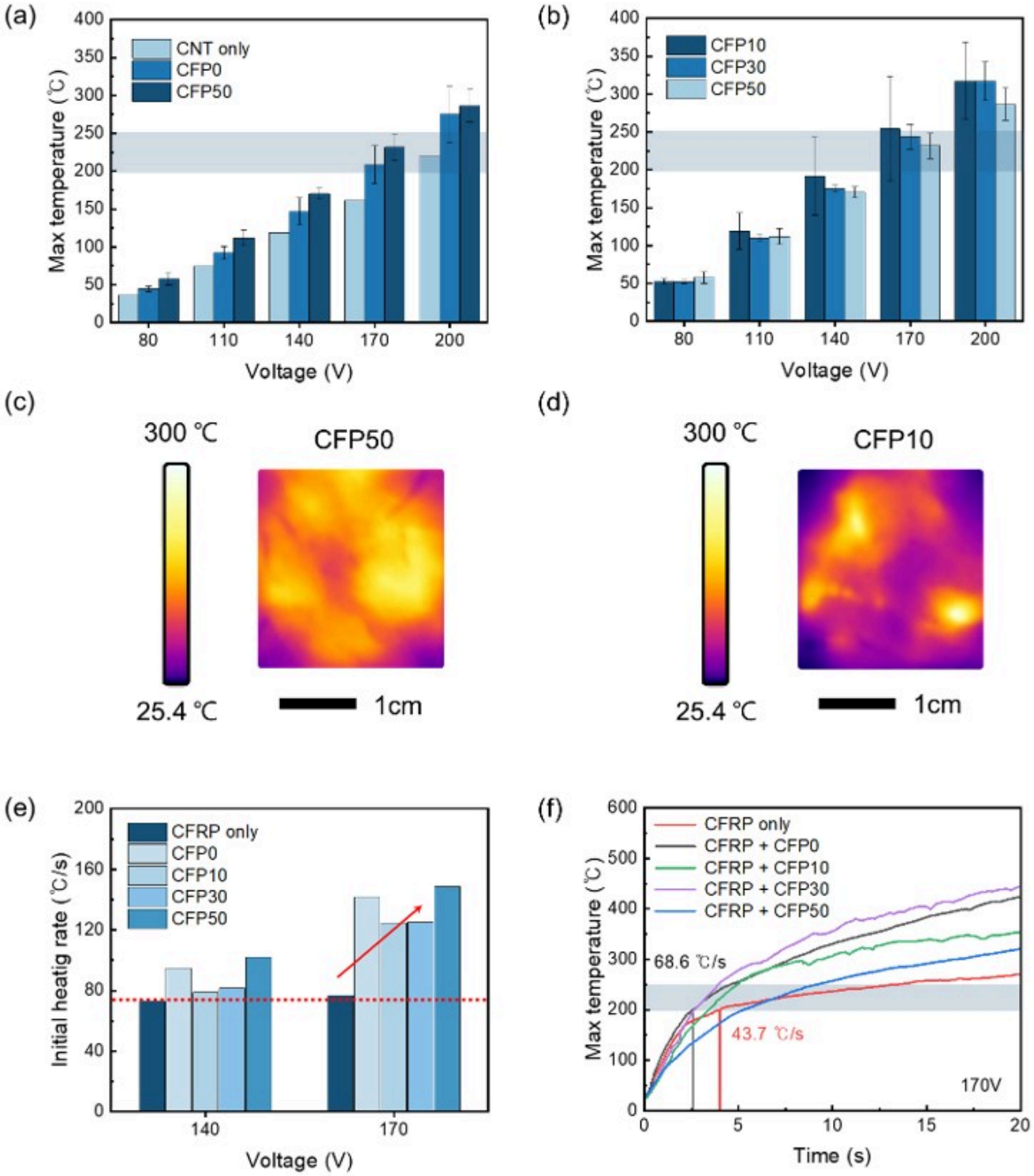


Figure 4

Induction heating behavior of CNT/Fe_3O_4/PA6 nanocomposites: (a) heating performance of the nanocomposite vs CNT-only; (b) as a function of PA6 content; (c) uniform heat distribution (CFP50); (d) non-uniform heat distribution (CFP10); (e) faster initial heating rate vs CFRP-only; (f) shorter time to PA6 melting temperature vs CFRP-only.

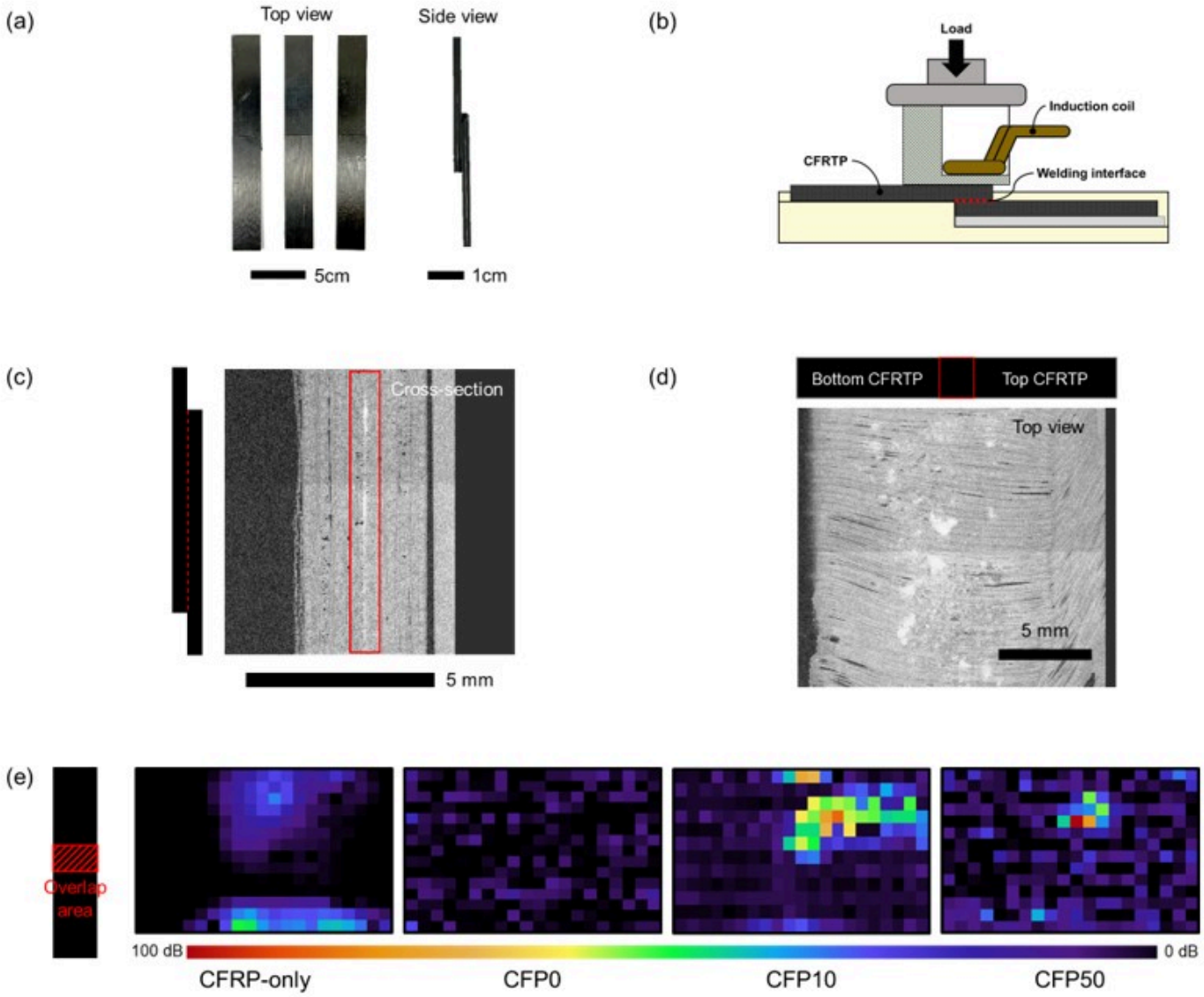


Figure 5

Application of CNT/Fe_3O_4/PA6 nanocomposites to induction welding: (a) assembly of CFRP; (b) schematic illustration of induction-welding setup; Micro-CT images of the CFP50 showing complete interfacial welding (c) the cross-section; (d) top view; (g) C-scan images of overlap area vs CFRP-only.

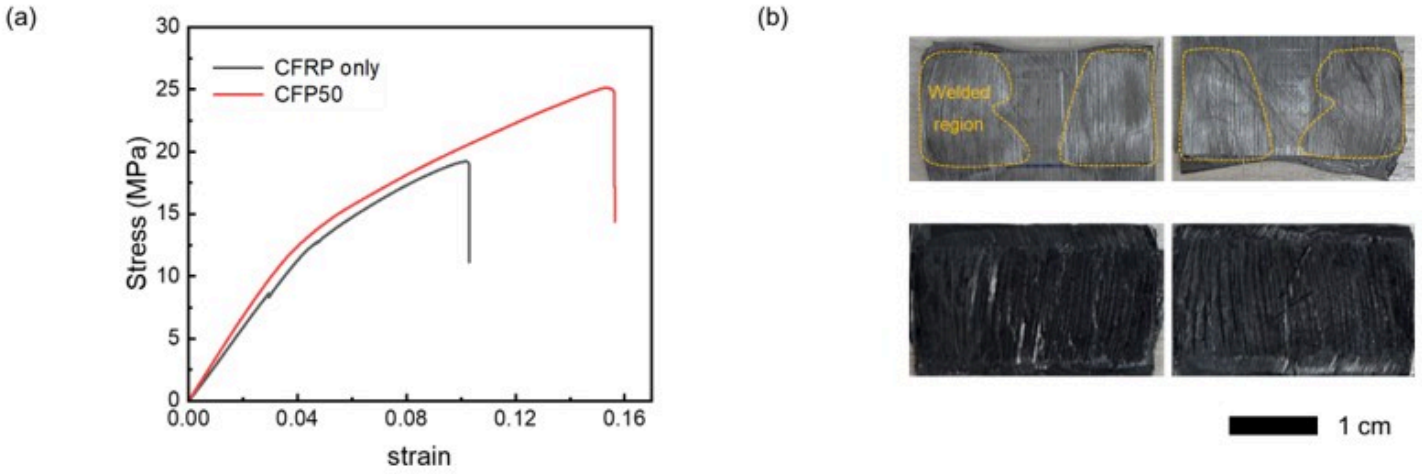


Figure 6

Mechanical strength test of fracture surface observations: (a) single lap shear strength vs CFRP-only; (b) fracture surfaces.

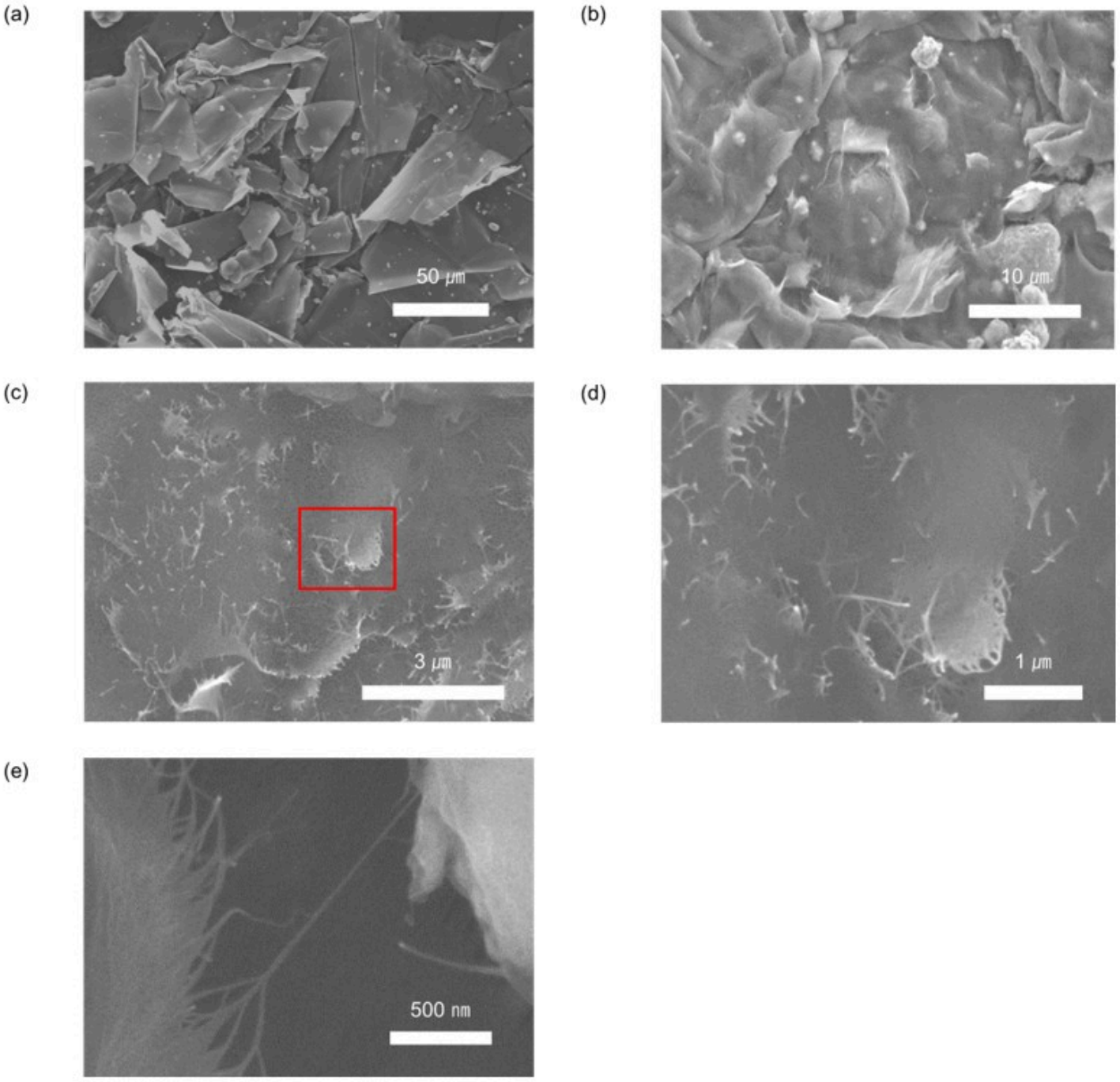


Figure 7

SEM images of fractured interfaces: (a) unwelded interlayer morphology; (b) welded interface with PA6 infiltration and residual polymer; (c,d) high-magnification views showing CNT pull-out; (e) pulled-out individual CNT.

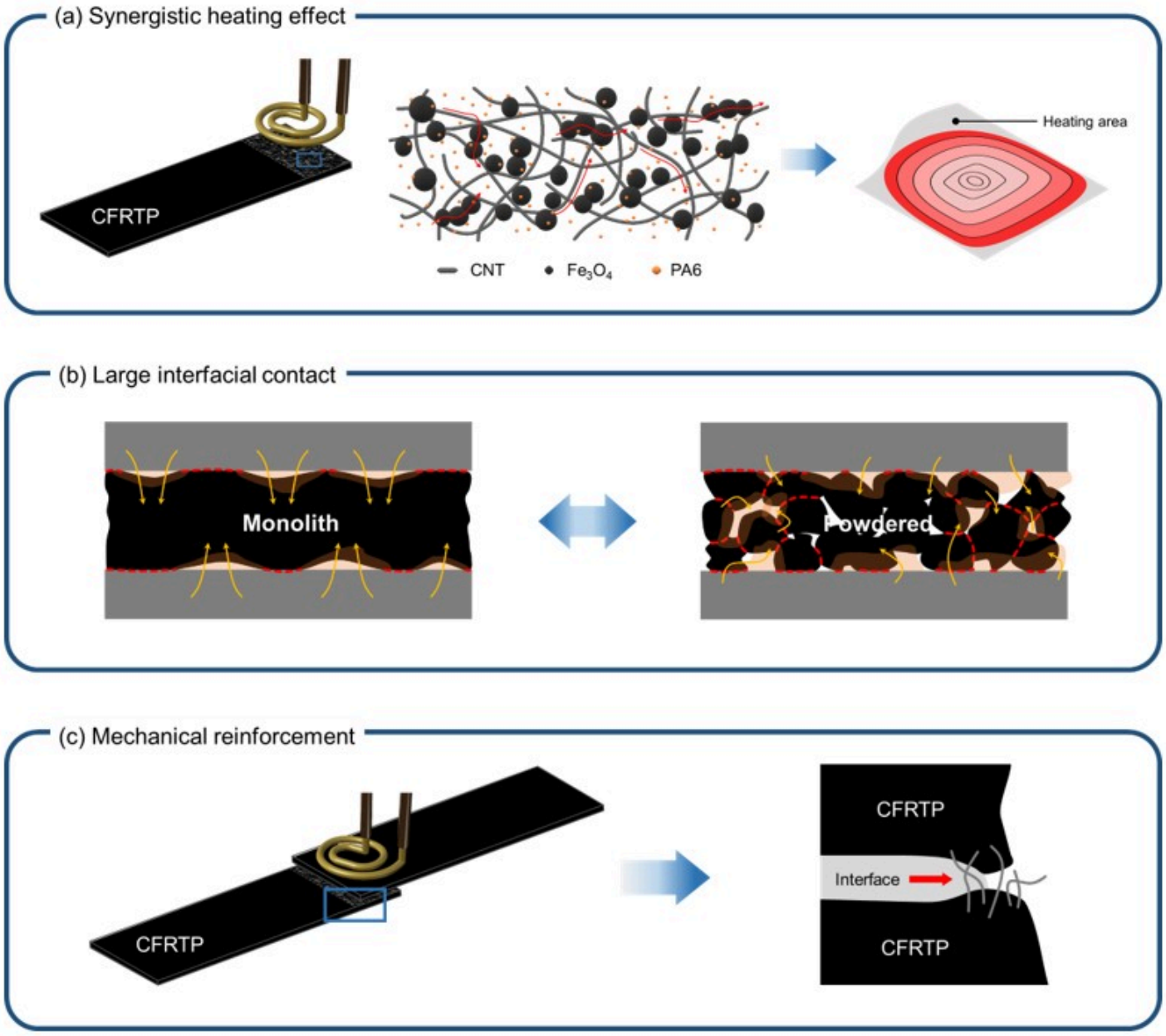


Figure 8

Schematic of proposed heating and welding mechanisms: (a) synergistic heating from CNT, Fe_3O_4, and PA6 losses; (b) comparison of interfacial contact in monolith and powder; (c) CNT pinning effect reinforcing the welded region.

Supplementary Files

This is a list of supplementary files associated with this preprint. Click to download.

- supplementarydata.docx